**ROYAL SOCIETY OF CHEMISTRY**

## PAPER

Check for updates

# Yolk–shell SnSe$_2$@NC nanocubes: synergistic interior void and spatial confinement for superior sodium-ion battery anodes†

Yanan Du,[a] Zhilong Wu,[b] Siying Wang,[b] Ran Sun,[b] Zhiya Lin, [iD][c] Hai Jia, [iD][c] Xiaohui Huang, [iD][b] Shaoming Ying*[b] and Zhiqiang Huang [iD] *[b]

Rationally designed nanostructured electrode materials, especially yolk–shell metal selenide@void@C architectures, are gaining prominence as potential anode candidates for sodium-ion batteries (SIBs) due to their exceptional sodium-ion storage capabilities. In this work, we propose a template-assisted carbon coating route to fabricate nitrogen-doped carbon nanocubes encapsulating SnSe$_2$ nanoparticles, forming a yolk–shell structure with an internal void space (SnSe$_2$@NC), resulting in a high-performance anode for SIBs. The yolk–shell architecture, with SnSe$_2$ nanoparticles embedded within a nitrogen-doped carbon shell, significantly boosts structural integrity and sodium storage performance. The SnSe$_2$@NC electrode delivers a high reversible capacity of 368.9 mA h g$^{-1}$ after 50 cycles at 0.5 A g$^{-1}$ and an impressive capacity retention of 324.2 mA h g$^{-1}$ at 5 A g$^{-1}$ after 1000 cycles. Electrochemical analyses reveal that the enhanced performance is attributed to the improved Na-ion diffusion kinetics, reduced charge-transfer resistance, and the structural stability conferred by the nitrogen-doped carbon shell and the internal void space. The yolk–shell SnSe$_2$@NC nanocubes demonstrate superior electrochemical properties, representing a potential strategy for the development of advanced SIB anode materials.

## 1. Introduction

With the increasing prominence of energy and environmental issues, the development of new energy sources and the promotion of electric vehicles are emerging as an inevitable trend.[1–3] The pursuit of advanced energy storage systems has led to a surge in the development of sodium-ion batteries (SIBs) as a viable alternative to lithium-ion batteries (LIBs), considering the abundance and cost-effectiveness of sodium resources and the similar working principles to those of LIBs.[4–6] Central to the high performance of SIBs are high-capacity anode materials that can endure the volumetric changes during sodium inter-calation and de-intercalation without sacrificing structural integrity.[7–9] However, the larger ionic radius of Na$^+$ compared to Li$^+$ leads to slower diffusion kinetics within anode materials during cycling, making some LIBs anode materials, such as

graphite, ineffective in SIBs.[10–13] Thus, developing high-performance anode materials for SIBs is a significant challenge.

Tin diselenide (SnSe$_2$), possessing a high theoretical capacity (756 mA h g$^{-1}$) and a large interlayer spacing, stands out as a potential anode material for SIBs. Despite this promise, its practical use faces challenges due to substantial volume expansion ($\approx$420%) and particles aggregation during cycling, which lead to rapid capacity fading and poor rate capability.[14,15] In recent years, considerable progress has been made by researchers in enhancing the sodium storage capabilities of SnSe$_2$ anode for sodium-ion batteries.[16–18]

In this context, the design of SnSe$_2$ based anode materials with structural features of accommodating volume changes and maintaining electronic and ionic conductivity is of crucial importance.[19–21] Wang *et al.*[22] proposed a self-templated strategy to fabricate porous carbon-fiber coated SnSe$_2$ nanoparticles (SnSe$_2$/NPC), which exhibited superior sodium storage performance in sodium-ion batteries (SIBs). The SnSe$_2$/NPC electrode demonstrated high reversible capacity, fast charge/discharge rate performance, and enduring cycling stability, delivering substantial desodiation capacities of 416, 396, 385, 365, 332, and 305 mA h g$^{-1}$ at current densities ranging from 0.1 to 5.0 A g$^{-1}$. The remarkable performance was ascribed to the interconnected and porous architecture of SnSe$_2$/NPC, which encapsulated SnSe$_2$ nanoparticles within a porous carbon-fiber network. The porosity of the structure facilitated sodium ion

*[a]College of Chemistry and Materials Science, Fujian Normal University, Fuzhou 350117, China*

*[b]College of New Energy and Materials, Ningde Normal University, Fujian Provincial Key Laboratory of Featured Materials in Biochemical Industry, Ningde 352100, China. E-mail: huangzq003@126.com; yingshaoming@126.com*

*[c]College of Mathematics and Physics, Ningde Normal University, Ningde, 352100, China*

diffusion, and the carbon-fiber layer enhanced electrical conductivity and maintained structural integrity. Park *et al.*[23] constructed a unique yolk–shell structured SnSeS@C anode with goat pupil-like configuration of S-doped SnSe yolk and a hollow carbon shell, showing superior electrochemical performance, with a long cycle life of 186 mA h g$^{-1}$ over 1000 cycles at 0.5 A g$^{-1}$ and a rate capability of 112 mA h g$^{-1}$ at 5 A g$^{-1}$. The sophisticated structure and composition contributed to the enhanced electrochemical properties of the SnSeS@C anode.

Based on the literature review, an innovative strategy involves the use of hollow structures to encapsulate SnSe$_2$ nanoparticles, providing a unique combination of interior void space for volume expansion and spatial confinement to maintain structural integrity. Additionally, incorporating an electrically conductive outer framework enhances both the electrical conductivity and chemical stability of the anode materials.[24] Chen *et al.*[25] developed a SnSe$_2$/C–N anode material derived from Sn-MOFs, demonstrating outstanding performance in SIBs with stable capacities of 259 mA h g$^{-1}$ at 0.1 A g$^{-1}$ after 100 cycles. The key advancements were the use of MOFs as precursors to create a robust carbon framework, the enhancement of electrical conductivity, and the improvement in structural stability through nitrogen doping. Song *et al.*[26] prepared SnSe/NC hollow nanospheres as SIB anodes with superior performance with 77.05% capacity retention (120.50 mA h g$^{-1}$) after 900 cycles at 1 A g$^{-1}$ and good rate capability, maintaining 285.69 mA h g$^{-1}$ at 100 mA h g$^{-1}$ after high-rate testing. The nitrogen-doped carbon matrix inhibited volume expansion and polyselenide loss, ensuring structural stability throughout cycling.

Incorporating heteroatoms like nitrogen into carbon to create a sturdy outer framework that encapsulates SnSe$_2$ nanoparticles with an internal void space is a strategic approach to enhance the electrochemical performance of SnSe$_2$. The nitrogen doping enhances the electronic conductivity of the carbon matrix, while the inner hollow structure provides mechanical support and limits the aggregation of SnSe$_2$ nanoparticles, ensuring uniform distribution of stress during the sodiation/desodiation processes. This design effectively alleviates the mechanical strain associated with volume changes, thereby prolonging the lifespan of the anode material and enhancing its rate capability.

In this research, nitrogen-doped carbon nanocubes were fabricated as a shell to encapsulate SnSe$_2$ nanoparticles (forming the yolk structure) with an internal void space (SnSe$_2$@NC) by combining a template method with a polydopamine pyrolytic carbon coating approach (see ESI†). Compared to pristine SnSe$_2$ without the nitrogen-doped carbon coating, the yolk–shell SnSe$_2$@NC nanocubes leverage the physical buffering and chemical bonding between the nitrogen-doped carbon matrix and SnSe$_2$ nanoparticles to suppress volume expansion and polyselenide loss, thereby achieving excellent long-term cycling stability for sodium storage. As a result, SnSe$_2$@NC exhibits outstanding electrochemical performance as an anode material for sodium-ion batteries (SIBs), with a high capacity of 368.9 mA h g$^{-1}$ at 0.5 A g$^{-1}$ and remarkable rate cycle stability,

retaining 324.2 mA h g$^{-1}$ at 5 A g$^{-1}$ after 1000 cycles. Moreover, the SnSe$_2$@NC electrode demonstrates superior rate capability, with discharge capacities of 395.0, 363.5, 356.7, 347.0, and 324.4 mA h g$^{-1}$ at current rates of 0.2, 0.5, 1, 2, and 5 A g$^{-1}$, respectively. We further discuss structural characterization and the mechanisms underlying the enhanced electrochemical performance of SnSe$_2$@NC, emphasizing the significance of structural design in the advancement of SIBs. This study is believed to offer valuable insights for the design and synthesis of high-performance metal selenide anodes for SIBs.

## 2. Results and discussion

Fig. 1 illustrates the schematic diagram of the controllable synthesis process for hollow nanocubes of SnSe$_2$@NC. Firstly, uniform ZnSn(OH)$_6$ nanocubes, approximately 100 nm in size, it were synthesized using the coprecipitation method (as the SEM picture shown in Fig. 2a). Then polydopamine (PDA) was *in situ* coated onto the ZnSn(OH)$_6$ nanocubes, constructing core–shell structured ZnSn(OH)$_6$@PDA nanocubes (as shown in Fig. 2b). Subsequently, ZnSn(OH)$_6$@PDA were calcined at 600 °C in an Ar atmosphere, which was then etched with HCl dissolution to remove impurities and produce SnO$_2$@NC hollow nanocubes (as shown in Fig. S1a†). Finally, SnO$_2$@NC hollow nanocubes and Se powders were thoroughly mixed and calcined to obtain SnSe$_2$@NC hollow microcubes (as shown in Fig. 2c). As a control sample, ZnSn(OH)$_6$ nanocubes without PDA coating were subjected to the same preparation process as the SnSe$_2$@NC to obtain pure SnSe$_2$ (as shown in Fig. S1b and c†). Due to the robust shell of the pyrolytic carbon from PDA, the nanocube structure remained intact even after the selenization process (Fig. 2c). Transmission electron microscopy (TEM) unveiled the inner architecture of the yolk–shell nanocubes (as depicted in Fig. 1d), showcasing a densely packed core encircled by a substantial void within the carbon shell, which measures approximately 10.9 nm in thickness. This observation is likely due to the fact that, during selenization under an Ar/H$_2$ atmosphere, SnO$_2$ is concurrently reduced to Sn, a metal with a melting point as low as 232 °C, leading to its evaporation and subsequent bead formation.[27,28] In the high-resolution TEM images presented in Fig. 2e and f, the SnSe$_2$ core exhibits distinct lattice fringes with an interplanar spacing of 0.191 nm, which matches the (110) plane of the hexagonal SnSe$_2$ crystal structure. The SAED patterns (Fig. 2g) clearly show diffraction rings of the (100) and (001) planes of hexagonal SnSe$_2$. Concurrently, elemental mapping (as shown in Fig. 2h–k) was utilized to examine the distribution of C, N, Sn, and Se within an individual yolk–shell nanocube. It is evident
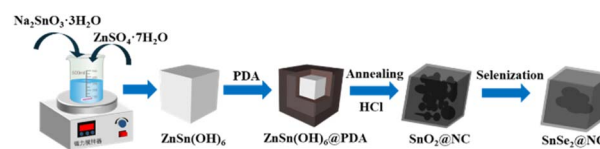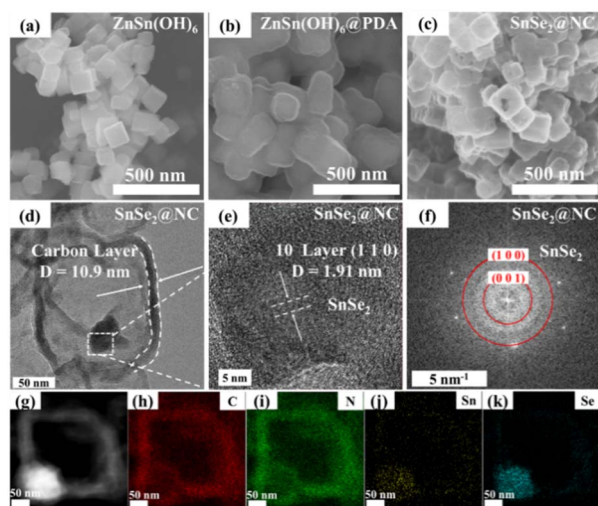


**Fig. 1** Schematic of formation process of Cube SnSe$_2$@NC.

Fig. 2 SEM images of (a) ZnSn(OH)$_6$, (b) ZnSn(OH)$_6$@PDA, (c) SnSe$_2$@NC, (d) TEM, (e and f) HRTEM, (g) SAED, (h–k) elemental mapping of SnSe$_2$@NC powders.



Fig. 3 (a) XRD patterns of SnSe$_2$@NC and SnSe$_2$; (b) Raman spectra test of the SnSe$_2$@NC materials; XPS survey spectrum of SnSe$_2$@NC and the corresponding high-resolution spectra of (c) C 1s, (d) N 1s, (e) Sn 3d, (f) Se 3d.

that the majority of Sn and Se elements are concentrated within the dense core of the hollow carbon shell, whereas C and N elements are predominantly found at the periphery. The N element is derived from the carbon residue resulting from the pyrolysis of PDA. Generally, the structure of large void space inside the N-rich carbon shell for SnSe$_2$-based anodes would be expected to have superior performance for sodium storage.[29,30]

The composition and crystal structure information of precursors, SnSe$_2$ and SnSe$_2$@NC were investigated using X-ray diffraction (XRD). Fig. 3a shows the XRD patterns of SnSe$_2$ and SnSe$_2$@NC. Both the diffraction peaks display the characteristic hexagonal SnSe$_2$ diffraction peaks (JCPDS No. 89-2939),[31] indicating the successful synthesis of SnSe$_2$@NC. The X-ray diffraction (XRD) patterns of the precursor of ZnSn(OH)$_6$ and intermediate product of SnO$_2$@NC are shown in Fig. S2.† In the Raman spectra (Fig. 3b), the SnSe$_2$@NC sample exhibits a pronounced peak at 1360 cm$^{-1}$, attributed to the D-band, and a significant peak at 1570 cm$^{-1}$, corresponding to the G-band of carbon.[32] The D-band typically originates from the carbon's defective and disordered structures, whereas the G-band is indicative of the sp$^2$-hybridized, graphitic carbon framework.[33] The intensity ratio of these peaks ($I_D/I_G$) serves as an indicator of defect concentration. Based on the area fitting analysis, SnSe$_2$@NC has an $I_D/I_G$ ratio of 2.3, which suggests a substantial presence of defects. X-ray photoelectron spectroscopy (XPS) spectra are also collected to further determine the bonding states and valence states of SnSe$_2$@NC (shown in Fig. S3†), presenting the signal at high resolution from C 1s, N 1s, Sn 3d, and Se 3d (Fig. 3c–f). As depicted in Fig. 3c, the high-resolution C 1s spectrum is primarily resolved into three distinct peaks. The peaks located at approximately 284.8 eV and 286.3 eV are attributed to C–C and C=O bonds, respectively.[34] In the N 1s spectrum presented in Fig. 2d, the peaks at 398.4 eV, 399.8 eV, and 400.7 eV correspond to pyridinic, pyrrolic, and graphitic nitrogen.[24,35] The existence of pyrrolic and graphitic nitrogen
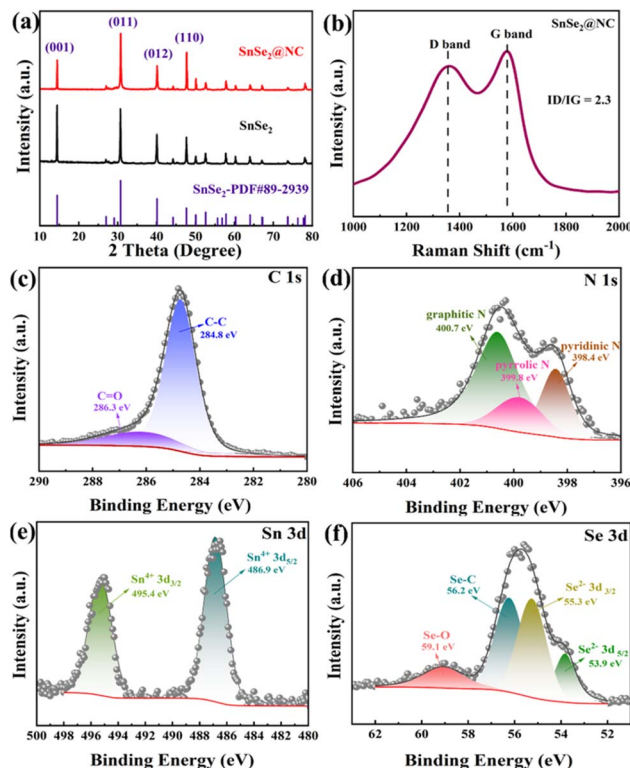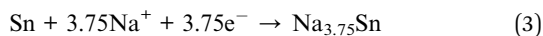
serves to create active sites that facilitate Na$^+$ intercalation and deintercalation, which in turn enhances the reaction kinetics and subsequently improves the rate performance of the battery.[36] Fig. 3e displays the high-resolution energy spectrum of Sn 3d, with characteristic peaks at 486.9 eV and 495.4 eV, which correspond to the binding energies of Sn$^{4+}$ 3d$_{5/2}$ and Sn$^{4+}$ 3d$_{3/2}$, respectively.[37] From the Se 3d high-resolution spectrum (Fig. 2f), four distinct peaks can be clearly identified, with two at 53.9 eV and 55.3 eV, which can be assigned to the Se$^{2-}$ 3d$_{5/2}$ and Se 3d$_{3/2}$ of Se$^{2-}$, respectively.[22,24] The peak at 59.1 eV is associated with Se–O bonds,[37] resulting from surface oxidation due to prolonged exposure to air. Meanwhile, the peak at 56.2 eV represents the binding energy of the Se–C bond.[38] It has been discussed that the Se–C bond plays a crucial role in battery performance, primarily by bolstering the structural stability of the electrode materials.[38–40]

The electrochemical performance of SnSe$_2$@NC as an anode for SIBs was elucidated using a half cell configuration with sodium metal foil as the counter electrode. For comparative analysis, SnSe$_2$ was also evaluated. Cyclic voltammetry (CV) was employed to elucidate the various electrochemical reactions occurring throughout the charge/discharge cycles recorded at the rate of 0.1 mV s$^{-1}$ over a potential range of 0.01–3.0 V. Drawing from prior research on SnSe$_2$ anodes for sodium storage, the initial charging process is believed to involve both intercalation and conversion reactions:[41]

$$xNa^+ + SnSe_2 + xe^- \rightarrow Na_xSnSe_2 \qquad (1)$$

$$4Na^+ + SnSe_2 + 4e^- \rightarrow 2Na_2Se + Sn \qquad (2)$$

$$Sn + 3.75Na^+ + 3.75e^- \rightarrow Na_{3.75}Sn \qquad (3)$$

The initial discharging process of the CV profile (Fig. 4a) exhibits a reduction peak near 1.65 V, which is associated with the intercalation of $Na^+$ into the interlayer space of $SnSe_2$ crystal structure with the formation of $Na_xSnSe_2$ (eqn (1)). The peak observed at 0.71 V (vs. $Na/Na^+$) corresponds to the formation of $SnSe_2$ to metallic Sn and $Na_2Se$, and the formation of irreversible solid electrolyte interphase (SEI) layer (eqn (2)). During the initial anodic sweep, the broad peaks at near 0.20 can be attributed to the conversion process from metallic Sn to $Na_{3.75}Sn$ (eqn (3)), while the peaks at 1.35 V and 1.55 V are indicative of the desodiation process, and the minor peak at 2.16 V (vs. $Na/Na^+$) is attributed to the reformation of $SnSe_2$.[40] It merits emphasis that the CV curve from the third cycle closely aligns with that of the second, signifying excellent reversibility in the sodium storage reaction of $SnSe_2@NC$.[42] By comparison, the bare $SnSe_2$ shares a similar CV profile with the $SnSe_2@NC$ composite (referring to Fig. S4†) during first scan, but the peak currents in the CV curves of $SnSe_2$ in the 2nd and 3rd cycles are considerably weaker compared to those of $SnSe_2@NC$. This indicates a poorer reversibility for $SnSe_2$, suggesting that the composite material outperforms the pure $SnSe_2$ under the same experimental conditions.

The results of the galvanostatic charge/discharge measurements are depicted in Fig. 4b and c. As shown in Fig. 4b, $SnSe_2@NC$ electrode demonstrates the superior electrochemical performance, achieving a high reversible capacity of 368.9 mA h $g^{-1}$ after 50 cycles at 0.5 A $g^{-1}$, much higher than that of pure $SnSe_2$ with a capacity of 159.0 mA h $g^{-1}$ at the same current density. As shown in Fig. S5,† $SnSe_2@NC$ delivers a specific discharge capacity value of 686.6 and a specific charge capacity value of 515.5 mA h $g^{-1}$, corresponding to a high initial coulombic efficiency (ICE) of 75.08% during the first cycle. For comparison, pure $SnSe_2$ delivers a specific discharge capacity value of 617.7 mA h $g^{-1}$ and a specific charge capacity value of 391.9 mA h $g^{-1}$ with an ICE of 63.44%. The observed capacity loss is attributed to the formation of an irreversible solid electrolyte interphase (SEI) film on the electrode surface and the decomposition of the electrolyte. Compared to pure $SnSe_2$ shown in Fig. 4c, $SnSe_2@NC$ also exhibits better rate capability and higher average capacity at different current densities.

As illustrated in Fig. 4c, we probed the rate performance of the $SnSe_2@NC$ electrode across a range of current densities from 0.2 to 5 A $g^{-1}$. The electrode exhibited average discharge capacities of 395.0, 363.5, 356.7, 347.0 and 324.4 mA h $g^{-1}$ at 0.2, 0.5, 1, 2 and 5 A $g^{-1}$, respectively. These values markedly surpass those of the pristine $SnSe_2$ electrode, which delivered 138.9, 109.1, 92.3, 76.5 and 59.6 mA h $g^{-1}$ under the same current densities. Notably, when the current density was reduced back to 0.2 A $g^{-1}$, the $SnSe_2@NC$ electrode's discharge capacity swiftly rebounded to approximately 470.6 mA h $g^{-1}$. EIS tests were measured to further investigate the reaction kinetics of $SnSe_2@NC$ and pure $SnSe_2$ electrodes to investigate the reaction kinetics for SIBs. As shown in Fig. 4d, each Nyquist plot is composed of a semicircle and a straight line. The semicircle, evident in the high and medium frequency ranges, is typically associated with the charge transfer impedance ($R_{ct}$) of the electrode. Conversely, the straight line observed in the low frequency range is ascribed to the Warburg impedance, which is indicative of mass transport limitations. The fitting results of equivalent circuits are shown in Table S1.† The charge transfer resistance ($R_{ct}$) of $SnSe_2@NC$ is 28.7 Ω, much lower than that of $SnSe_2$ ($R_{ct}$ = 127.8 Ω), indicating that existence of N doped carbon layer improves the electronic conductivity of $SnSe_2@NC$. As detailed in the quantitative data of the low-frequency region (Table S1†), the $SnSe_2@NC$ electrode exhibits reduced charge transfer impedance and accelerated ion diffusion compared to the pure $SnSe_2$, thereby enhancing the reaction kinetics.[43,44] To delve deeper into the assessment of the sustainable stability, endurance, and structural integrity of $SnSe_2@NC$ and pristine $SnSe_2$, high current density of 5 A $g^{-1}$ was applied after the cells activated at 0.1 A $g^{-1}$ for the starting 10 cycles (Fig. 4e). The discharge capacity of $SnSe_2@NC$ electrode sustains at 324.2 mA h $g^{-1}$ after 1000 cycles at 5 A $g^{-1}$, much higher than that of $SnSe_2$ with a discharge capacity of 52.7 mA h $g^{-1}$ after 200 cycles. The yolk–shell-structured $SnSe_2@NC$ exhibited enhanced structural integrity following electrochemical reactions, which was instrumental in its exceptional stable cycling
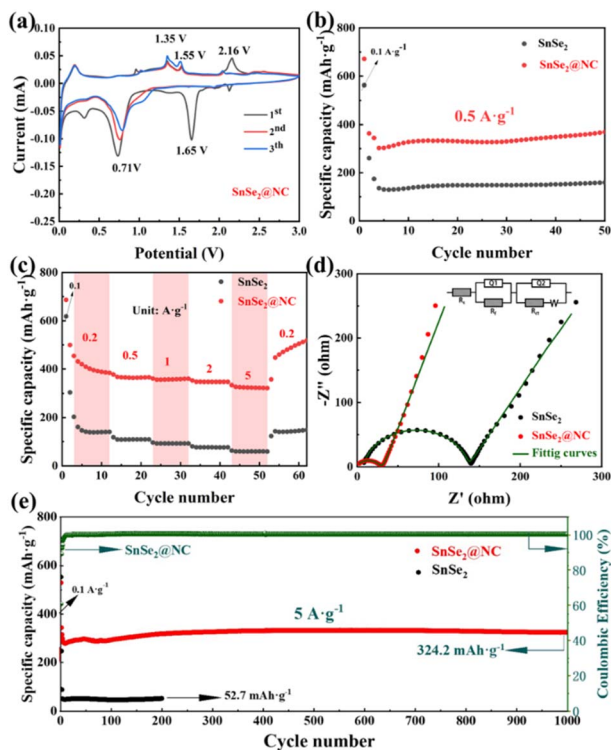


Fig. 4 Electrochemical performances of $SnSe_2@NC$ as anode materials. (a) CV curves of $SnSe_2@NC$ at 0.1 mV s$^{-1}$ with in 0.01–3.00 V, (b) cycling performance at 0.5 A g$^{-1}$, (c) rate capabilities at various current densities from 0.2 to 5 A g$^{-1}$, (d) EIS curves and (e) long-term cyclic capability at 5 A g$^{-1}$ of $SnSe_2$ and $SnSe_2@NC$.

performance. Conversely, the electrochemical behavior of pure SnSe$_2$ underscored its structural fragility, leading to a precipitous decline in capacities over cycling and diminished reversible capacities in subsequent cycles.

To elucidate the exceptional electrochemical performance of SnSe$_2$@NC electrode, cyclic voltammetry (CV) tests were conducted at various scan rates ranging from 0.1 to 1.0 mV s$^{-1}$, as depicted in Fig. 5a. The CV curves are fundamentally aligned with the expected profiles, indicating a swift charge transfer within SnSe$_2$@NC during the alloying and dealloying processes. The electrode's reaction kinetics and sodium storage mechanism can be explored by using the relationship between the measured current ($i$) and the related scanning rate ($v$):[45]

$$i(V) = av^b \tag{4}$$

in which $a$ is a constant, and $b$ is a constant for the same reaction and has to do with the energy storage reaction's starting components. When the value of $b$ is 1, the reaction has surface-controlled capacitive behavior, when the value is 0.5, the reaction is wholly a diffusion-controlled Faraday process. As shown in Fig. 5b, the $b$ values corresponding to different peaks in SnSe$_2$@NC are 0.89, 1.08, 1.00, 1.09, 0.99, 0.76 and 1.01, respectively. The overall value of $b$ is close to 1 indicating the dominant contribution of the pseudocapacitance. Furthermore, the contribution ratio of pseudocapacitance can be calculated based on the response current composed ($i(V)$) of pseudocapacitance contribution ($k_1v$) and diffusion-controlled insertion process ($k_2v^{1/2}$), which can be expressed by their relationship as follows:[45]
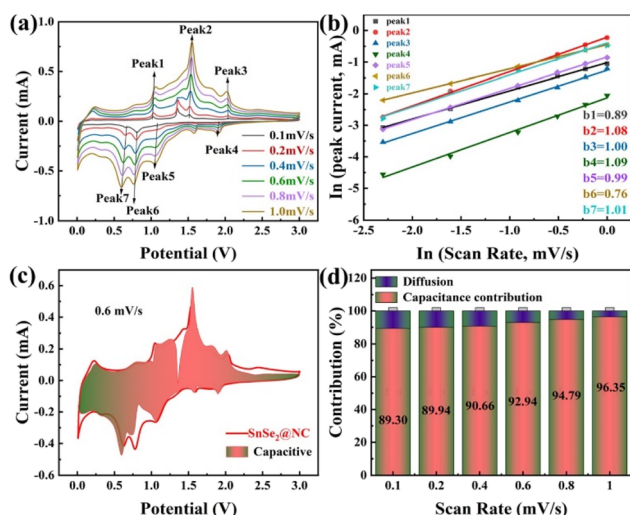
$$i(V) = k_1v + k_2 v^{1/2} \tag{5}$$

By fitting calculations, $k_1$ can be calculated, and based on it, the proportion of pseudocapacitance at each scanning speed can be calculated. As shown in Fig. 5c, the red shaded area of the CV is the pseudocapacitive contribution area (92.94%), which is mainly the pseudocapacitive contribution at 0.6 mV s$^{-1}$. As indicated in Fig. 5d, the capacitance contributions at scanning speeds of 0.1, 0.2, 0.4, 0.6, 0.8, and 1 mV s$^{-1}$ are 89.30%, 89.94%, 90.66%, 92.94%, 94.79%, and 96.35%, respectively. The significantly higher contribution of pseudocapacitance in SnSe$_2$@NC suggests that the dominant energy storage behavior is governed by pseudocapacitive effects, thereby endowing SnSe$_2$@NC with the capability to facilitate rapid Na$^+$ transmission and exhibit excellent high-speed cycling stability. In order to further illustrate the superior ions diffusion process, the diffusion coefficients of Na$^+$ ($D_{Na^+}$) were evaluated by the galvanostatic intermittent titration technique (GITT) test (Fig. S6†), the detailed calculation process is based on eqn (6).

$$D_{Na^+} = \frac{4}{\pi\tau}\left(\frac{m_b V_M}{M_b s}\right)^2 \left(\frac{\Delta E_s}{\Delta E_\tau}\right)^2 \tag{6}$$

Here, $D_{Na^+}$ denotes the Na$^+$ diffusion coefficient (cm$^2$ s$^{-1}$), $V_M$ is the molar volume, $\tau$ signifies the pulse duration, $m_b$ indicates the active mass of the electrode, $M_b$ is the molar mass of the electrode material, $s$ is the total surface area of the electrodes, $\Delta E_s$ represents the steady-state voltage variation attributed to the pulse ($V$) and $\Delta E_\tau$ corresponds to total cell voltage change during constant pulse time.[46] Fig. S6a† presents the potential response curves for both the charging and discharging processes of SnSe$_2$@NC and pure SnSe$_2$ in the initial cycle. Fig. S6b† illustrates the sodium diffusion behaviors of SnSe$_2$@NC and pure SnSe$_2$ during the Na$^+$ insertion and extraction processes. In summary, yolk–shell SnSe$_2$@NC nanocubes distinctly showed a higher average diffusion coefficient than pure SnSe$_2$. This highlights the superior electrochemical performance of SnSe$_2$@NC, where SnSe$_2$ nanoparticles encapsulated within an inner void space are enveloped by a nitrogen-doped carbon shell, conferring high electrical conductivity. The improved Na-ion diffusion kinetics of the SnSe$_2$@NC nanocubes results in a superior rate performance as anode for SIBs.

The solid electrolyte interphase (SEI) is crucial for maintaining both the performance and stability of anode materials for SIBs. It serves as a protective barrier that insulates the electrolyte from the electrode, thereby preventing undesired reactions and the subsequent degradation during electrochemical reaction process.[47] A robust and well-formed SEI film is indispensable for sustaining the energy density, extending the lifespan, and ensuring the overall safety of the battery.[38,48] To further gain a better understanding the origin of the excellent electrochemical performances of SnSe$_2$@NC and pure SnSe$_2$, XPS characterizations of electrodes after cycling was carried out (Fig. 6). As depicted in Fig. 6a and b, the distinct C 1s spectrum peaks for SnSe$_2$@NC and pure SnSe$_2$ were resolved into three peaks at approximately 288.6, 285.8, and 284.8 eV, corresponding to CO$_3^{2-}$, C–O–C, and C–C, respectively.[49] In the O 1s XPS spectrum as shown in Fig. 6c and d, the peaks at 531.7,



Fig. 5 (a) CV curves of the SnSe$_2$@NC electrode in the Na coin-cell at various scan rates from 0.1 to 1 mV s$^{-1}$, (b) calculation of $b$-values using the relationship of the scan rate and peak current, (c) the CV curve of the SnSe$_2$@NC electrode at 0.6 mV s$^{-1}$ with the separation of capacitive and diffusion currents, (d) contribution ratio of the capacitive and diffusion controlled capacity at different scan rates.
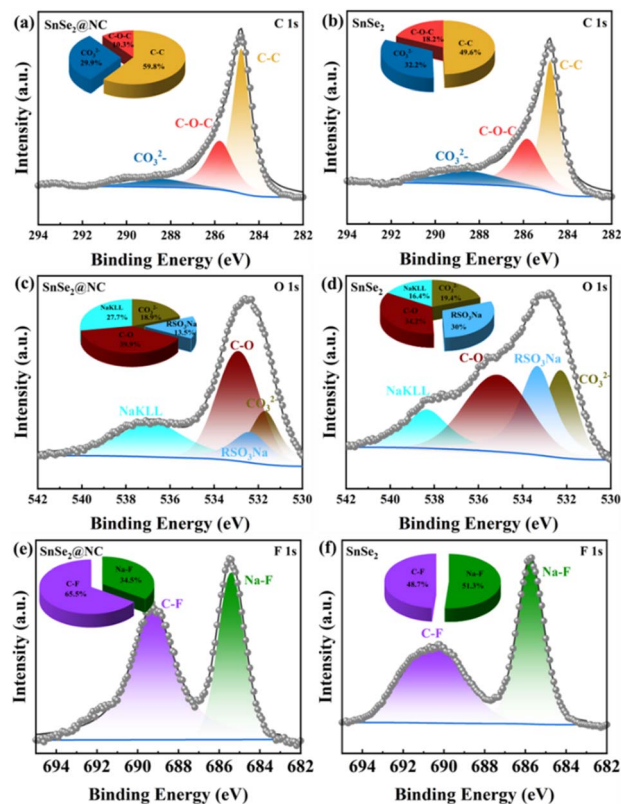
**Fig. 6** (a and b) C 1s, (c and d) O 1s (e and f) F 1s XPS of SnSe$_2$ and SnSe$_2$@NC extract from the electrode after the first charge and discharge, respectively.

532.5, 532.9, and 536.9 eV correspond to CO$_3^{2-}$, RSO$_3$Na, C–O, and NaKLL, respectively. The detection of RSO$_3$Na and Na$_2$CO$_3$ in both the O 1s and C 1s XPS spectra is indicative of the reduction derived from NaCF$_3$SO$_3$ electrolyte within diethylene glycol dimethyl ether. However, it is important to highlight that these compounds are thermodynamically unstable.[24] As an adverse outcome of this side reaction, RSO$_3$Na and Na$_2$CO$_3$, which possess inferior electronic and ionic conductivities, lead to heightened electrode polarization. This, in turn, exacerbates the kinetics of Na$^+$ diffusion, ultimately degrading the system's overall performance. In comparison to pristine SnSe$_2$ electrodes, SnSe$_2$@NC exhibits significantly lower levels of RSO$_3$Na and Na$_2$CO$_3$, indicating that the SnSe$_2$ nanoparticles confined within nitrogen-doped carbon nanocubes featuring inner void spaces could effectively minimize side reactions and facilitate the formation of a more stable SEI layer. Consequently, this configuration helps prevent the growth of sodium dendrites and enhances the overall lifespan of the electrodes.

The F 1s spectra depicted in Fig. 6e and f reveal two distinct peaks corresponding to C–F and Na–F bonds, which serve as evidence for the presence of NaF and C–F species within the SEI film on the electrodes. The formation of these NaF and C–F species is believed to stem from the decomposition of NaCF$_3$-SO$_3$.[50] It is evident that the modified SnSe$_2$@NC has a reduced content of Na–F bonds compared to the pristine SnSe$_2$ electrode. This indicates that the N-doped carbon layer can effectively

inhibit the decomposition of NaCF$_3$SO$_3$ during the sodiation/desodiation process. In summary, the SEI layer of the SnSe$_2$@NC electrode is significantly more stable than that of the pristine SnSe$_2$ electrode throughout the entire sodiation/desodiation process. This enhanced stability suggests that the SnSe$_2$@NC yolk–shell nanocubes has improved Na$^+$ diffusion kinetics, likely owing to its structural robustness and excellent conductivity. Consequently, the SnSe$_2$@NC electrode shows superior capacity retention, particularly at high current densities.

## 3. Conclusions

In conclusion, the yolk–shell SnSe$_2$@NC nanocubes with a nitrogen-doped carbon shell and internal void space have proven to be an outstanding anode material for SIBs, providing high specific capacity, superior rate performance and enduring cycling stability. Electrochemical analysis revealed that the observed improvements could be attributable to enhanced sodium-ion diffusion kinetics, diminished charge-transfer impedance, and bolstered structural stability, which are consequences of the nitrogen-doped carbon shell and the presence of internal void spaces. Additionally, XPS results of electrodes after cycling confirm the formation of a stable solid electrolyte interphase layer of SnSe$_2$@NC, crucial for battery performance and safety. The structural design and material composition of SnSe$_2$@NC provide valuable insights for the development of high-performance anode materials for next-generation energy storage systems.

## Data availability

The data used in this study is available upon request from the corresponding author.

## Conflicts of interest

There are no conflicts to declare.

## Acknowledgements

## References

1 G. W. Gao, X. M. Huo, B. X. Li, J. X. Bi, Z. K. Zhou, Z. Z. Du, W. Ai and W. Huang, *Energy Environ. Sci.*, 2024, **17**, 7850–7859.

2 H. J. Li, X. Q. Cheng, J. Y. Zhao, M. Y. Gao, H. Xu and X. M Wang, *J. Alloys Compd.*, 2025, **1010**, 178237.

3 J. . M. Tao, J. J. Han, Y. B. Wu, Y. M. Yang, Y. Chen, J. X. Li, Z. G. Huang and Y. B. Lin, *Energy Storage Mater.*, 2024, **64**, 103082.

4 J. L. Liang, C. B. Wei, D. X. Huo and H. Li, *J. Energy Storage*, 2024, **85**, 111044.

5 Z. W. Hu, L. Y. Liu, X. Wang, Q. Q. Zheng, C. Han and W. J. Li, *Adv. Funct.*, 2024, **34**, 2313823.

6 B. W. Xiao, T. Rojo and X. L. Li, *ChemSusChem*, 2019, **12**, 133–144.

7 Z. Y. Lin, J. S. Wu, Z. L. Wu, M. X. Yu, H. Jia, K. Q. Zhou, X. H. Huang and S. M. Ying, *J. Energy Storage*, 2025, **106**, 114924.

8 L. Wang, Z. X. Wei, M. L. Mao, H. X. Wang, Y. T. Li and J. M. Ma, *Energy Storage Mater.*, 2019, **16**, 434–454.

9 H. Li, Y. Y. He, Q. Wang, S. N. Gu, L. Wang, J. X. Yu, G. W. Zhou and L. Q. Xu, *Adv. Energy Mater.*, 2023, **13**, 2302901.

10 H. J. Li, X. M. Wang, Z. X. Zhao, R. Pathak, S. Y. Hao, X. M. Qiu and Q. Q. Qiao, *J. Mater. Sci. Technol.*, 2022, **99**, 184–192.

11 Y. Jiang, Y. C. Wang, J. F. Ni and L. Li, *InfoMat*, 2021, **3**, 339–352.

12 J. M. Tao, L. W. Liu, J. J. Han, J. J. Peng, Y. Chen, Y. M. Yang, H. R. Yao, J. X. Li, Z. G. Huang and Y. B. Lin, *Energy Storage Mater.*, 2023, **60**, 102809.

13 H. H. Kim, T. H. Kim, G. B. Cho, H. S. Ryu and J. H. Ahn, *J. Energy Storage*, 2024, **76**, 109848.

14 M. H. Luo, H. X. Yu, F. Y. Hu, T. T. Liu, X. Cheng, R. T. Zheng, Y. Bai, M. Shui and J. Shu, *Chem. Eng. J.*, 2020, **380**, 122557.

15 M. J. Liu, J. L. Xu, L. Y. Shao, X. Y. Shi, C. S. Li and Z. P. Sun, *Chem. Commun.*, 2024, **60**, 6860.

16 Y. T. Gong, Y. Li, M. Q. Liu, Y. Bai and C. Wu, *Small*, 2023, **19**, 2206194.

17 H. H. Li, L. F. Zhai, J. M. Yu, J. H. Luo, B. H, C. H. Hou, Y. M. Han, W. B. Pei and W. W. Xiong, *ACS Appl. Energy Mater.*, 2024, **7**, 9255–9266.

18 T. W. Zhao, G. Q. Feng, L. L. Zhou, X. Wang, X. Q. Li, F. Jiang, H. Y. Li, Y. S. Liu, Q. Yu, H. J. Gao, Y. Xu and Y. Y. Zhu, *ACS Appl. Nano Mater.*, 2024, **7**, 13434–13446.

19 S. Tian, X. Cheng, H. Li, M. Wang and X. Wang, *Mater. Today Chem.*, 2023, **30**, 101524.

20 W. W. Wang, L. J. Hu, L. X. Li, C. X. Liu, X. J. Liu, H. Wang and G. H. Zhai, *Electrochim. Acta*, 2023, **449**, 142239.

21 F. Zhang, Y. Shen, M. Shao, Y. C. Zhang, B. Zheng, J. S. Wu, W. N. Zhang, A. P. Zhu, F. W. Huo and S. Li, *ACS Appl. Mater. Interfaces*, 2020, **12**, 2346–2353.

22 C. Wang, L. Z. Sheng, M. H. Jiang, X. R. Lin, Q. Wang, M. Q. Guo, G. Wang, X. M. Zhou, X. Zhang, J. Y. Shi and L. L. Jiang, *J. Power Sources*, 2023, **555**, 232405.

23 G. D. Park and Y. C. Kang, *Small Methods*, 2021, **15**, 2100302.

24 Z. Y. Lin, J. S. Wu, Q. W. Ye, Y. L. Chen, H. Jia, X. H. Huang and S. M. Ying, *Dalton Trans.*, 2024, **53**, 765–771.

25 Z. Y. Chen, Z. Zhang, L. Z. Wang, Y. F. Li, Y. T. Wang, Y. C. Rui, A. l. Song, M. Li, Y. Y. Chu, L. Jiang, B. H. J. Tang, N. H, G. X. Wang and H. Tian, *Nanoscale*, 2024, **16**, 14339–14349.

26 H. H. Song, Q. Zhou, Z. C. Song, K. Tian, C. H. Guan, Z. Y. Fang, G. Y. Yuan, M. Lu, D. Wei and X. D. Li, *Dalton Trans.*, 2023, **52**, 14088–14099.

27 H. An, M. Yoo, H. Ha, H. Choi, E. Kang and H. Y. Kim, *Sci. Rep.*, 2019, **9**, 16702.

28 H. Ha, M. Yoo, H. An, K. Shin, T. Han, Y. Sohn, S. Kim, S. R. Lee, J. H. Han and H. Y. Kim, *Sci. Rep.*, 2017, **7**, 14427.

29 F. J. Kong, Z. S. Han, S. Tao and B. Qian, *J. Energy Chem.*, 2021, **55**, 256–264.

30 S. H. Xiao, Z. Z. Li, J. T. Liu, Y. S. Song, T. S. Li, Y. Xiang, J. S. Chen and Q. Y. Yan, *Small*, 2020, **16**, 2002486.

31 P. Liu, J. Han, K. J. Zhu, Z. H. Dong and L. F. Jiao, *Adv. Energy Mater.*, 2020, **10**, 2000741.

32 Z. Y. Lin, X. Q. Tan, Y. P. Lin, J. P. Lin, W. Y. Yang, Z. Q. Huang, S. M. Ying and X. H. Huang, *RSC Adv.*, 2022, **12**, 28341.

33 Z. H. Sun, X. L. Wu, J. N. Xu, D. Y. Qu, B. L. Zhao, Z. Y. Gu, W. H. Li, H. J. Liang, L. F. Gao, Y. Y. Fan, K. Zhou, D. X. Han, S. Y. Gan, Y. W. Zhang and L. Niu, *Small*, 2020, **16**, 1907670.

34 Y. Xin, S. Pan, X. Z. Hu, C. Miao, S. Q. Nie, H. Y. Mou and W. Xiao, *J. Colloid Interface Sci.*, 2023, **639**, 133–144.

35 D. Li, J. Q. Zhang, S. M. Ahmed, G. Q. Suo, W. Wang, L. Feng, X. J. Hou, X. H. Ye and L. Zhang, *J. Colloid Interface Sci.*, 2020, **574**, 174–181.

36 H. J. Wang, J. L. Lan, H. C. Yuan, S. C. Luo, Y. Q. Huang, Y. H. Yu, Q. Cai and X. P. Yang, *Appl. Surf. Sci.*, 2020, **518**, 146221.

37 H. Li, Y. Y. He, Q. Wang, S. N. Gu, L. Wang, J. X. Yu, G. W. Zhou and L. Q. Xu, *Adv. Energy Mater.*, 2023, **13**, 2302901.

38 K. W. Yang, X. X. Zhang, L. M. Song, J. Y. Zhang, C. T. Liu, L. W. Mi, Y. Y. Wang and W. H. Chen, *Electrochim. Acta*, 2020, **337**, 135783.

39 Y. Y. Wang, F. Y. Xiao, X. Chen, P. X. Xiong, C. Y. Lin, H. E. Wang, M. D. Wei, Q. R. Qian, Q. H. Chen and L. X. Zeng, *InfoMat*, 2023, **5**, e12467.

40 F. Zhang, C. Xia, J. J. Zhu, B. Ahmed, H. F. Liang, D. B. Velusamy, U. Schwingenschlögl and H. N. Alshareef, *Adv. Energy Mater.*, 2016, **6**, 1601188.

41 D. L. Cheng, L. C. Yang, R. Z. Hu, J. W. Liu, R. C. Che, Y. N. Chen, W. Y. Chen, J. L. Huang, M. Zhu and Y. J. Zhao, *ACS Appl. Mater.*, 2019, **11**, 36685–36696.

42 Z. L. Wu, Z. Q. Huang, M. X. Yu, Y. N. Du, J. W. Li, H. Jia, Z. Y. Liu, X. H. Huang and S. M. Ying, *Dalton Trans.*, 2024, **53**, 15920–15927.

43 X. C. Ren, J. S. Wang, D. M. Zhu, Q. W. Li, W. F. Tian, L. Wang, J. B. Zhang, L. Miao, P. K. Chu and K. F. Huo, *Nano Energy*, 2018, **54**, 322–330.

44 T. T. Wang, K. W. Ynag, J. Shi, S. R. Zhou, L. W. Mi, H. P. Li and W. H. Chen, *J. Energy Chem.*, 2020, **46**, 71–77.

45 H. H. Liu, D. Li, H. L. Liu, X. Wang, Y. X. Lu, C. Wang and L. Guo, *J. Colloid Interface Sci.*, 2023, **634**, 864–873.

46 W. F. Fan, J. P. Xue, D. P. Wang, Y. X. Chen, H. . B. Liu and X. H. Xia, *ACS Appl. Mater. Interfaces*, 2021, **13**, 61055–61066.

47 L. W. Ji, M. Gu, Y. Y. Shao, X. L. Li, M. H. Engelhard, B. W. Arey, W. Wang, Z. M. Nie, J. Xiao, C. M. Wang, J. G. Zhang and J. Liu, *Adv. Mater.*, 2014, **26**, 2901–2908.

48 S. K. Heiskanen, J. J. Kim and B. L. Lucht, *Joule*, 2019, **3**, 2322–2333.

49 J. Sun, L. A. O'Dell, M. Armand, P. C. Howlett and M. Forsyth, *ACS Energy Lett.*, 2021, **6**, 2481–2490.

50 K. Varghese, D. S. Baji, S. Nair and D. Santhanagopalan, *Front. Mater. Sci.*, 2022, **16**, 220601.